Plasma Sources Science and Technology

PAPER • OPEN ACCESS

Effect of the cathode surface temperature on the cathode fall layer parameters: experiment and simulation

To cite this article: Leanid Simonchik *et al* 2024 *Plasma Sources Sci. Technol.* **33** 025014

View the article online for updates and enhancements.

You may also like

- Transitions of an atmospheric-pressure diffuse dielectric barrier discharge in helium for frequencies increasing from kHz to MHz
J-S Boisvert, J Margot and F Massines
- New DDSCR structure with high holding voltage for robust ESD applications
Zi-Jie Zhou, , Xiang-Liang Jin et al.
- Exploration to generate atmospheric pressure glow discharge plasma in air
Wenzheng LIU, , Chuanlong MA et al.

This content was downloaded from IP address 144.122.201.61 on 04/03/2024 at 16:20

OPEN ACCESS
IOP Publishing
Plasma Sources Science and Technology
Plasma Sources Sci. Technol. **33** (2024) 025014 (15pp)
https://doi.org/10.1088/1361-6595/ad2580

Effect of the cathode surface temperature on the cathode fall layer parameters: experiment and simulation

Leanid Simonchik[1], **Mikalai Tomkavich**[1], **Gubad Islamov**[2], **Ender Eylenceoglu**[2] **and Ismail Rafatov**[2,3,*]

[1] Stepanov Institute of Physics, NAS of Belarus, pr. Nezavisimostsi 68-2, 220072 Minsk, Belarus
[2] Department of Physics, Middle East Technical University, Ankara 06800, Turkey
[3] School of Physics, Harbin Institute of Technology, Harbin 150001, Heilongjiang, People's Republic of China

E-mail: rafatov@metu.edu.tr

Received 18 August 2023, revised 11 January 2024
Accepted for publication 2 February 2024
Published 16 February 2024

Abstract

Combined experimental and numerical studies reveal a significant effect of the cathode temperature on the basic parameters (such as the electric field profile, thickness of the cathode fall layer, current density, and gas temperature) of the cathode fall of the self-sustained normal direct current atmospheric pressure glow discharge (APGD) in helium. Numerical models are spatially one- and two-dimensional and based on drift-diffusion theory of gas discharges. It was observed that heating of the cathode, resulting from a flow of the discharge current in APGD with a constricted positive column, leads to an increase of the interelectrode voltage if the cathode is not cooled and its temperature increases. With additional heating of the cathode by an external heat source, the interelectrode voltage tends to decrease. Radially inhomogeneous profiles of the reduced electric field on the uncooled cathode surface were measured. Simulation results exhibit reasonably good agreement with experiment for APGDs with cooled and uncooled cathodes.

Keywords: gas discharge, helium, atmospheric pressure plasma, Stark broadening, glow discharge, numerical simulation

1. Introduction

Nowadays, various types of gas discharges are widely used as sources of non-equilibrium atmospheric pressure plasma [1–6]. The direct current (DC) atmospheric pressure glow discharges (APGDs) attract particular interest because of their simple design, which dispenses with the need for a vacuum chamber. The enormous heat release at such high (atmospheric) pressures makes it necessary to cool the electrodes in these gas discharges. This heat release is likely the reason that most relevant studies were limited to discharge currents of less than one hundred milliamperes [7–9]. In fact, effective cooling of the cathode allows to extend the operating current range of the APGDs up to 10 A [10–15]. Therefore, controlling the cathode temperature and maintaining it constant in these discharge systems is of considerable importance.

More generally, the efficient use of APGD as a plasma source in applications implies an understanding of the dependence of plasma parameters in the discharge on external factors. The temperature regime on the cathode can be considered as one of them. The results of numerous studies [14, 16–20] indicate a significant effect of the cathode temperature on the

* Author to whom any correspondence should be addressed.

Original Content from this work may be used under the terms of the Creative Commons Attribution 4.0 licence. Any further distribution of this work must maintain attribution to the author(s) and the title of the work, journal citation and DOI.

© 2024 The Author(s). Published by IOP Publishing Ltd

glow discharge parameters. In particular, there are both theoretical and experimental data suggesting its effect on the interelectrode voltage. Indeed, according to numerical modelling of a low-pressure glow discharge in [14], an increase in the gas temperature results in an increase in the discharge sustaining voltage at a fixed discharge current and gas pressure. Furthermore, for an abnormal glow discharge at low pressure, experimental results [16] showed that the interelectrode voltage for a glow discharge with a cathode cooled with liquid nitrogen differs from that for a discharge with an uncooled cathode by several hundred volts at a discharge current of 5 mA. As shown in [13], the heating of the cathode leads to a change in the cathode fall parameters. More specifically, the excess (by about 400 K) of the uncooled cathode temperature over the cooled one results in an increase in the interelectrode voltage by 70–80 V at a constant discharge current of 1 A, as well as in an increase in the thickness of the cathode fall layer by one and a half times.

However, despite a large amount of research conducted in this area, the fundamental mechanisms driving APGDs are not yet fully understood. Indeed, we could not find any references suggesting an answer to the question of why the interelectrode voltage increases when the cathode surface temperature rises. The results of a systematic analysis of the influence of the cathode temperature on the APGD parameters were reported in experimental works [13, 15], however, without providing any explanations and interpretations of this phenomenon. In addition, different interelectrode gaps and conditions were employed in those experiments, making the results difficult to interpret. The present study intends to (at least partially) compensate for this lack of knowledge and contribute to a better understanding of the role of gas temperature in APGDs. Therefore, this work provides further development of the study [13], under the similar experimental conditions, including also one- and two-dimensional numerical analysis. The aim is to gain further insight into the effect of the cathode temperature on the APGD parameters, in particular, in the cathode fall layer.

As the analysis of numerous models for glow discharges shows [21], even at low pressures, these models lead to discrepancies in the prediction of the parameters of the cathode layer. This is partly due to uncertainties in the exact mechanisms and parameters quantifying the electron emission properties of the cathode, as well as the lack of reliable data on the collision cross-sections of elementary processes in plasma. However, numerical studies and simulations of high (atmospheric) pressure gas discharges impose much higher demands on the reliability and adequacy of the corresponding numerical models. The numerical model applied in this work is based on a fluid description of charged and neutral particles and a drift-diffusion approximation of particle fluxes. Within this approach, the electron kinetic coefficients (the electron transport coefficients as well as the rate constants of the electron induced elementary reactions) are defined as functions of the electron temperature, using a solution of the electron Boltzmann equation and corresponding collision cross-sections [22–24]. The spatial profile of the electron temperature is found by solving the electron energy balance equation, which is incorporated into the model. The model, developed and implemented in this work for the APGD, basically follows the approach from [25, 26] with respect to the plasma composition and the set of corresponding plasma-chemical reactions.

The paper is organized as follows. The current state of the art of the experimental studies is described in section 2. The numerical model is presented and the simulation results are reported in section 4. The discussions are given in section 5. Finally, section 6 contains the conclusions.

2. State of affairs regarding experimental studies

2.1. Experimental setup

The experimental setup used in this study is similar to that of [13]. Glow discharge is ignited between two electrodes in an air-locked chamber with quartz glass windows. The discharge chamber dimensions are $100 \times 100 \times 70$ mm^3. A weak flow of working gas (about 1 l min^{-1}) is provided through the discharge chamber. The step-up transformers with typical bridge rectifiers and capacitive filtering are used in power supplies. The output voltage is varied from 0 to 3 kV and the ballast resistor can be changed from several tens of kΩ at low currents (less than 100 mA) to 100 Ω at high discharge currents (greater than 100 mA).

A flat copper cathode is used in the experiments. Its diameter is about 36 mm, which is larger than the observed diameter of the negative glow, i.e. the effects associated with an abnormal discharge are excluded.

The discharge is characterized by using the emission spectroscopy. A scanning 0.5 m high resolution (two gratings with 1800 grooves/mm) monochromator (SOL Instruments) was used for the spectral decomposition of the APGD emission. The monochromator was backed by an ICCD (Andor Technology, iStar DH340T). The inverse linear dispersion was $\sim$0.5 nm mm^{-1}, and the halfwidth of the Gaussian instrumental profile was equal to $\Delta\lambda_a \approx 0.03$ nm.

In this work we used Stark polarization spectroscopy using the He I $(2p^1\mathrm{P}_0 - 4d^1\mathrm{D})$ transition with its forbidden component He I $(2p^1\mathrm{P}_0 - 4f^1\mathrm{F})$ emitting at 492.2 nm. In the presence of an external electric field, the dipole forbidden component starts emitting and the emission becomes polarized. The resulting local electric field and polarization-dependent Stark splitting and shifting of the atomic emission lines allows us to determine the local electric field from the changes in the spectral line profiles [27–29]. The resolved rotational bands of nitrogen ion (0,1) N_2^+ $(B^2\sum_u^+ - X^2\sum_g^+)$ and hydroxyl radical (0,0) OH $(A^2\sum^+ - X^2\Pi_\mathrm{i})$ were used to determine the gas temperature T_g [30].

2.2. The main parameters of the APGD in helium

The glow discharges maintained in the gap of 10 mm at different currents under intensive cooling of the cathode were considered in [10, 13]. Such cooling is especially necessary

Table 1. The main parameters of the APGD in helium (according to [10, 13]).

	Cooled	Uncooled
Discharge current	1 A	1 A
Interelectrode gap	10 mm	10 mm
Interelectrode voltage	220 V	300 V
Current density on cathode (average)	2.3 A cm^{-2}	~0.4 A cm^{-2}
Current density in positive column (average)	~20 A cm^{-2}	~20 A cm^{-2}
Gas temperature (negative glow)	600 K	1000 K
Gas temperature (middle of positive column)	~2300 K	~2300 K
Cathode temperature	~400 K	~800 K

at discharge currents greater than 0.5 A: the positive column is constricted at currents higher than 0.05 A. The current–voltage characteristic (CVC) of this discharge is falling with the increasing current, and the glow-to-arc transition occurs at currents greater than 10 A [10]. The electric field strength remains constant along the cathode surface.

In the case of an uncooled cathode, the difference in the positive column is not significant; substantial changes are observed mainly in the cathode region. Indeed, the negative glow area is increased by almost an order of magnitude. The electric field strength in this situation is not constant along the cathode surface; it decreases by a factor of 2–3 towards the periphery of the discharge [10, 13, 15].

The main parameters of the APGD in helium according to data from [10, 13, 15] are presented in table 1. It should be noted that an increase in the interelectrode voltage by about 80 V in the APGD with an uncooled cathode is associated with changes in the cathode fall region.

3. The high current APGDs with constricted and diffused positive columns

3.1. Current–voltage characteristics

Our previous experiments [10, 12, 13] were carried out under slightly different experimental conditions, specifically, the gas gaps. Although the length of the positive column, in general, has practically no effect on the main parameters of the cathode fall region, nevertheless, it contributes to the inhomogeneity of the spatial distribution of temperature in this region and the heating of the cathode in high-current constricted and diffuse discharges. In addition, it should be pointed out that creating APGD with a diffuse positive column in a large gap at a high current is a difficult task even in helium. With these issues in mind, for definiteness, in the present study the experiments were performed with the same interelectrode gap of 5 mm. Images of helium APGD for different currents at this interelectrode gap are shown in figure 1. Different pairs of electrodes were used in the experiment:

(a) a water cooled copper cylinder 36 mm in diameter and rounded tungsten rod of 6 mm in diameter,
(b) uncooled flat copper disk 8 mm thick and 36 mm in diameter and rounded tungsten rod of 6 mm in diameter, and
(c) two uncooled flat copper disks 8 mm thick and 36 mm in diameter.

In cases (a) and (b), a tungsten rod was used as an anode, to prevent random movement of the discharge on the electrode surface, which is typical in the case of two flat electrodes.

Images of discharges at the current of 1 A and different gas gaps are shown in figure 2. It can be seen that at this current, the discharge with a diffuse positive column can be maintained at gaps less than about 5 mm, and it constricts at larger gaps. The average current density on the cathode during the transition from a diffuse to a constricted discharge varies from ~0.3 to ~0.4 A cm^{-2}. It should be noted that it is not possible to register the CVC of the diffuse discharge for a wide range of discharge currents, because the current decrease, at a given gas gap, is usually accompanied with a transition to the constricted mode. An interelectrode voltage of a diffuse discharge at a current of 1 A is about 326 V. It is pointed in figure 3 by a star symbol, wherein the voltage decreases by about 30 V at the transition from the diffuse discharge to the constricted one.

Figure 3 shows CVCs of discharges depicted in figure 1. In the case of a cooled cathode (figure 3, triangles) voltage is dropping, and this drop is determined by a positive column [13]. The average current density on the cathode for the current range under consideration is about 2 A cm^{-2}.

In the case of an uncooled cathode (figure 3, circles), CVC curve has a non-monotonic shape. It is dropping only at low currents. It stops dropping at currents higher than 0.2 A and rises sharply at currents of about 1 A, wherein a current density on the cathode reduces from 2 A cm^{-2} at low currents down to ~0.4 A cm^{-2} at currents higher 1 A. As it can be seen from figure 3, at the current of 1 A, an interelectrode voltage in the case of the uncooled cathode is about 70 V higher than that with the cooled cathode.

3.2. Spatial distribution of gas temperature

Discharges operating in diffuse and constricted modes, and with cooled and uncooled cathodes, which are different in appearance (see figures 1 and 2), apparently have different spatial heat release in the interelectrode gap, which will be reflected on the spatial distributions of gas temperature. The gas temperature was determined by using the resolved rotational band ($B^2\sum_u^+ - X^2\sum_g^+$) of nitrogen ions N_2^+.

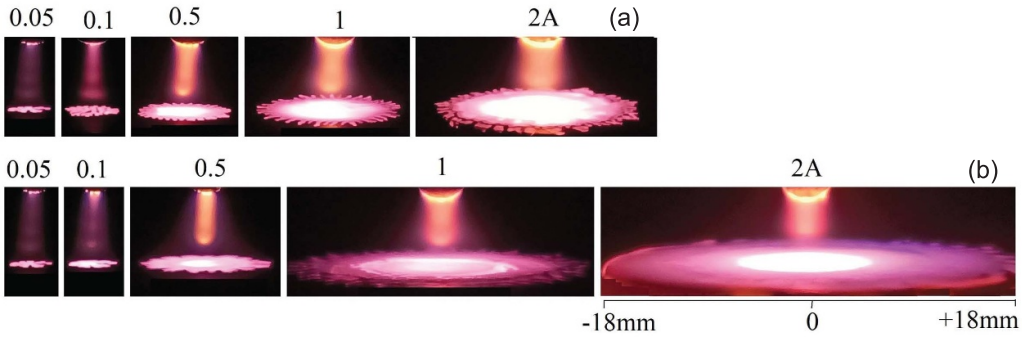

Figure 1. The images of helium APGDs with cooled (a) and uncooled (b) cathode for different discharge currents. The gas gap is 5 mm.

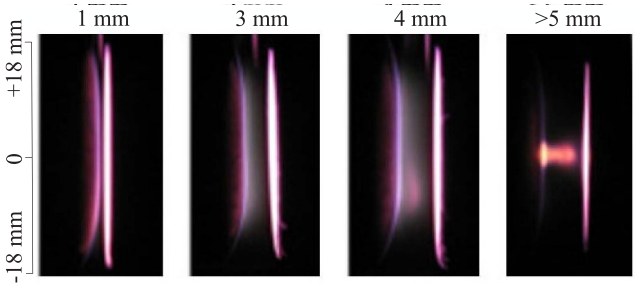

Figure 2. The images of helium APGDs for different interelectrode gaps. The transition from a diffuse to a constricted regime occurs at gaps larger than 5 mm. The discharge current is 1 A.

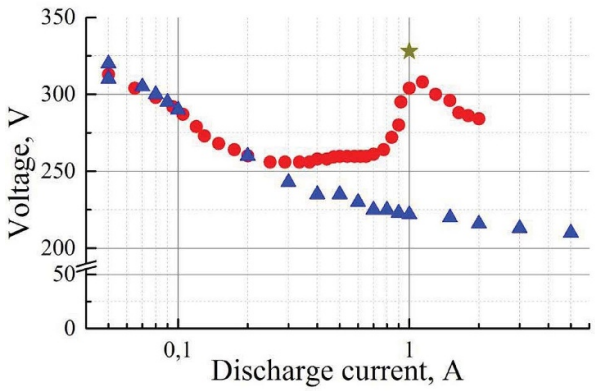

Figure 3. Current–voltage characteristics of constricted APGDs in helium with cooled (triangles) and uncooled (circles) cathodes from figure 1. The star symbol indicates the interelectrode voltage of diffuse APGD at current of 1 A. The gas gap is 5 mm.

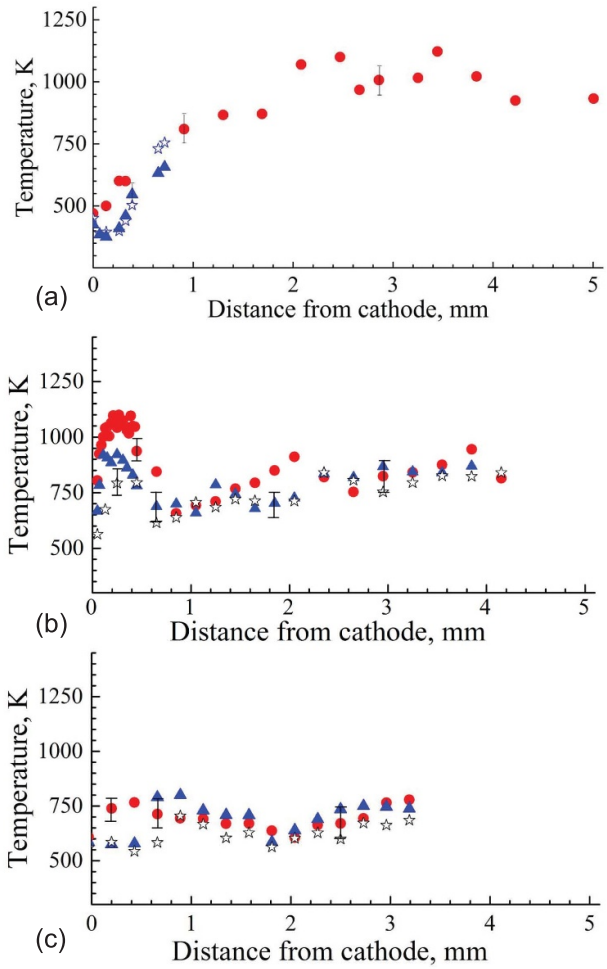

Figure 4. Longitudinal temperature profiles in the constricted APGD with cooled (a) and uncooled cathodes (b) and in the diffuse mode (c). Circles correspond to the axial temperature profiles, triangles to the profiles at a distance of one half of the corresponding negative glow radius, and stars to the edge of negative glow. Diameters of negative glow are 9 mm (a), 18 mm (b) and 36 mm (c). The discharge current is 1 A. The gas gap is 5 mm.

Let us consider the longitudinal distributions of gas temperature on the axis of discharges and away from the axis. In the case of a cooled cathode, the diameter of the negative glow is about 9 mm. Temperature distributions were obtained at a distance of one half of the negative glow radius and at the edge of negative glow (2.5 mm and 4.5 mm from the axis). They are presented in figure 4(a) along with the axial distribution. At the end of the cathode fall layer (~ 0.01 cm) the gas temperature is about 500 K for the discharge with a cooled cathode (circles). The temperature significantly increases with the distance from the cathode. This fact indicates that there is a heat flux from the positive column to the cathode layer.

If the cathode is not cooled, the diameter of the negative glow is about 18 mm. Longitudinal distributions were determined at distances from the axis of 4.5 mm and 9 mm. These distributions are presented in figure 4(b). As can be seen, the gas temperature on the axis of cathode reaches about 1100 K and decreases to ∼700 K in the Faraday dark space (FDS). Further it increases slightly towards the anode. A temperature peak at a distance of 2 mm from the cathode surface corresponds to the beginning of a positive column. In the temperature distribution at a distance of 4.5 mm from the axis, the temperature does not change in the FDS, while in the cathode region it decreases by 200 K. In the case of a distribution at 9 mm from the axis, the gas temperature in the cathode region decreases by another 200 K.

The situation is different in the case of diffuse discharge (figure 4(c)). The negative glow occupies the entire surface of the cathode, the diameter of which is 36 mm. Longitudinal temperature distributions were determined at distances of 8 mm and 16 mm from the axis. It can be seen that throughout the whole discharge gap space the temperature stays nearly the same (about 700 K).

It should be noted that the gas temperature near the surface of the uncooled cathode is in the range of 700–800 K for both contracted and diffuse discharges (figures 4(b) and (c)). For a cooled cathode it is lower, 450–500 K (figure 4(a)). In addition, based on the results in figure 4, we can also conclude that the gas temperature does not practically change along the cathode surfaces for each of the cases considered.

Let us estimate the current densities on the cathode. As follows from table 1, the average current density on the cathode in the constricted helium APGD at a current of 1 A is about 0.4 A cm^{-2} for an uncooled and 2.3 A cm^{-2} for a cooled copper cathode. In a diffuse APGD (figure 2) with an uncooled cathode, it is even smaller, less than 0.3 A cm^{-2}. Let us recalculate the values of the current density and thickness of the cathode fall for a diffuse discharge at a pressure of 1 Torr by using the classical scaling laws. For the atmospheric pressure, $p = 760$ Torr, we set the temperature equal to $T_g = 800$ K, and for the pressure of $p = 1$ Torr, we set $T_g = 290$ K. As a result of the rescaling, we obtain a current density of about 4×10^{-6} A cm^{-2} under classical glow discharge conditions. Rescaling the cathode fall thickness ∼0.01 cm to the classical discharge conditions yields a value of about 2.5 cm. Thus, the obtained values differ by less than two times from the current density of 2.2×10^{-6} A cm^{-2} and the cathode fall thickness of 1.3 cm corresponding to the classical glow discharge with an iron cathode [12]. Consequently, the parameters of the near-cathode region in a diffuse APGD more or less fit the scaling laws. In the case of the constricted APGD, the similar situation is observed at the periphery of the cathode fall region and a mismatch at its center due to an increase in the cathode fall voltage.

As shown in [9], even at low discharge currents (of the order of several milliamperes), there exists a heat flow from the positive column to the near-cathode region. For a helium APGD at a current of 1 A, according to [31], the heat flux to the cathode is about 250 W cm^{-2}. At the same time, the electric field strength in the positive column is about 100 V cm^{-1} and the current density is 20 A cm^{-2} [8]. Consequently, the volumetric power density is 2 kW cm^{-3}. For a positive column with a diameter of 3.5 mm and a length of 5 mm, the heat generation is of the order of 100 W. If at least half of this power is directed towards the cathode, then the heat flux through the cross-section of the positive column is about 500 W cm^{-2}. This value is comparable to the heat flux due to a heat release in the near-cathode region. Thus, in a constricted helium APGD with an uncooled cathode, gas heating in the central part of the near-cathode region occurs due to heat release both from the near-cathode region and from the positive column (figure 4(b)). This leads to additional heating of the cathode.

A gas heating at the cathode fall layer edge is due to heat release in this region and additional heat flux from cathode, a surface temperature of which will be comparable with the surface temperature at the center due to high heat conductivity of copper. We can consider a gas heating from cathode as external additional heat source. In the case of a cooled cathode, since an effective cooling provides heat removal, the difference does not matter and current density is about 2.3 A cm^{-2} along whole cathode surface.

An experiment with the heating of the cathode in APGD in helium was performed in [15]. It has been established that the heating of the cathode with an external heat source in glow discharge in normal regime leads to a decrease in voltage by 20–30 V at a current of 50 mA. In addition, the presence of a heat flow from the positive column to the cathode fall region was observed.

3.3. Spatial distributions of electric field strength

Let us now compare the profiles of the electric field strength in the cathode fall for the constricted discharges with cooled and uncooled cathodes and a diffuse discharge with an uncooled cathode. We used Stark polarization spectroscopy using the He I ($2p^1P_0 - 4d^1D$) transition with its forbidden component He I ($2p^1P_0 - 4f^1F$) emitting at 492.2 nm. Images of He I 492.2 nm line profiles above the cathode surface (at a distance of about 20 μm) for the three discharges registered by ICCD camera are shown in figure 5. The brighter narrow vertical stripes in the figure centers correspond to the unshifted component, the radiation of which comes from regions of the discharge, where the electric field is practically absent. To the left of the unshifted component locates the forbidden component, and to the right is the allowed one. Vertical direction indicates the distance along the cathode surface.

In the case of a constricted discharge with a cooled cathode (figure 5(a)), the strips of the forbidden and allowed lines are practically parallel up to the edge of the cathode potential fall region. This indicates a constant value of the electric field strength along the surface, which was demonstrated in [13]. In the case of a contricted discharge with an uncooled cathode (figure 5(b)), the forbidden and allowed components are most separated at the discharge axis. Towards the edge of the cathode fall region they come closer, which indicates a decrease in the electric field strength. In a diffuse discharge (figure 5(c)),

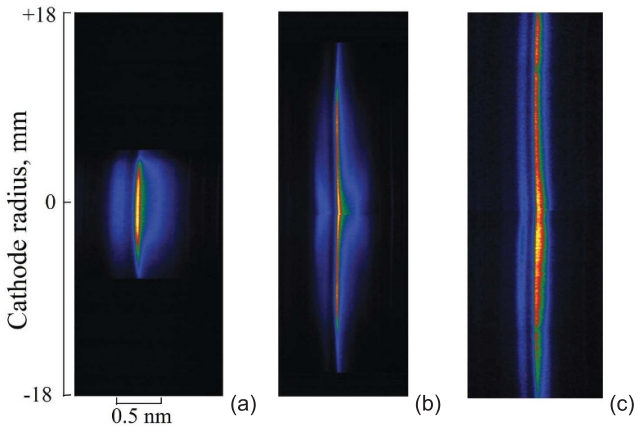

Figure 5. Images of He I 492.2 nm line profiles near the cathode surface: constricted discharge with a cooled cathode (a), constricted (b) and diffuse (c) discharges with an uncooled cathode. The discharge current is 1 A, the interelectrode gap is 5 mm. Vertical dimensions are 10 mm for the image (a) and 20 mm for the images (b) and (c).

the bands of the forbidden and allowed components are parallel along the whole surface of the cathode. The electric field magnitude is somewhat less than in a constricted discharge.

According to [10, 15], the electric field strength in the cathode fall of the discharge with a cooled cathode is constant in the radial direction and linearly drops in the axial direction from 60 kV cm^{-1} on the cathode surface to zero at distance of 70 microns from the cathode, which defines the cathode fall thickness (see figure 7(b)). In this case, the cathode fall voltage is about 210 V, which is somewhat larger than the classical value of 177 V for a pair of copper–helium.

In the case of an uncooled cathode, the electric field strength on axis drops linearly in axial direction also from 60 kV cm^{-1} at the cathode surface, but becomes close to zero at a distance of 100 microns from the cathode (figure 7(c)). Therefore, the thickness of the cathode fall increases by a factor of about 1.5. At the periphery of the cathode fall layer, the electric field strength drops linearly from 20 kV/cm at the cathode surface and becomes close to zero at a distance of about 120 microns from the cathode (figure 7(c)). The values of the voltage drop can be estimated from figure 7: it is about 115 V at the cathode periphery, and about 300 V on the discharge axis. As it was shown in [11], in the discharge with a constricted positive column (the gas gaps are larger than 1 mm), the heat flux from the positive column to the cathode region takes place even at discharge currents of several milliamperes. This additional heat flux leads to an increase in both the gas temperature in the cathode fall region, which is not related to the cathode fall voltage, and the thickness of the cathode fall layer. Ultimately, this leads to an increase in the interelectrode voltage. At the periphery of the cathode fall layer, the heat flux directed to the cathode is insignificant, and the temperature of the cathode surface remains approximately equal to the temperature on the cathode axis due to the high thermal conductivity of copper.

As for the diffuse discharge (figure 5(c)), the electric field strength on the cathode is about 20 kV cm^{-1} and it is the same along whole cathode surface. The thickness of cathode fall layer is about 120 microns.

4. Computational approach

In this section, the effect of cathode heating on the parameters of the discharge is investigated numerically. For this purpose, we used the COMSOL Multiphysics computational package (version 6.1) [32]. More precisely, numerical models of the APGD were developed using the 'General Form PDE' interface of this package and numerical solutions were obtained by applying time-dependent solver. Since we are interested in stationary states of the APGD, the solver was run until steady-state solutions were achieved.

The numerical description of a gas discharge plasma at high (atmospheric) pressure requires a special treatment. The numerical model is based on the LMEA ('local mean energy approximation') approach, which is also known as an 'extended fluid model' in the literature [22–24, 33]. Within this method, the electron kinetic coefficients (the transport (mobility and diffusion) coefficients as well as the rate constants of the electron induced plasma-chemical reactions) are calculated as functions of the electron energy (temperature), by using solution of the kinetic Boltzmann equation and corresponding electron collision cross-sections.

The parallel-plate geometry of the discharge system is considered. Numerical model is spatially two-dimensional, taking into account axial symmetry (see figure 6). We also carried out calculations for a spatially one-dimensional model, restricting an analysis to a direction normal to the electrode surfaces.

4.1. Numerical model

4.1.1. Governing Equations. The gas discharge model includes the continuity equations for plasma species

$$\frac{\partial n_j}{\partial t} + \nabla \cdot \mathbf{\Gamma}_j = S_j, \tag{1}$$

where $\mathbf{\Gamma}_j$ is the particle flux density in the drift-diffusion approximation,

$$\mathbf{\Gamma}_j = \mathrm{sgn}\,(q_j)\, n_j \mu_j \mathbf{E} - \nabla D_j n_j, \tag{2}$$

the Poisson's equation for the electrostatic field,

$$\epsilon_0 \nabla \cdot \mathbf{E} = \sum_j q_j n_j, \quad \mathbf{E} = -\nabla \phi, \tag{3}$$

the equation for the electron energy density

$$\frac{\partial n_\varepsilon}{\partial t} + \nabla \cdot \mathbf{\Gamma}_\varepsilon = -e\mathbf{\Gamma}_\mathrm{e} \cdot \mathbf{E} - \frac{3}{2}\frac{m_\mathrm{e}}{m_\mathrm{g}} \nu_\mathrm{ea} n_\mathrm{e} k_\mathrm{B} \left(T_\mathrm{e} - T_\mathrm{g}\right) - \sum_k \Delta E_k R_k, \tag{4}$$

and the energy balance equation to account for the effect of background gas heating

$$c_{\mathrm{p}}\frac{\partial(\rho T_{\mathrm{g}})}{\partial t}-\nabla(\lambda\nabla T_{\mathrm{g}})=e\boldsymbol{\Gamma}_{\mathrm{i}}\cdot\mathbf{E}+\frac{3}{2}\frac{m_{\mathrm{e}}}{m_{\mathrm{g}}}\nu_{\mathrm{ea}}n_{\mathrm{e}}k_{\mathrm{B}}(T_{\mathrm{e}}-T_{\mathrm{g}}). \quad (5)$$

In these equations, n denotes the species density, ϕ and $\mathbf{E}$ are the electric potential and field, T is the kinetic temperature, q is the electric charge, m is the particle mass, μ and D are the mobility and diffusion coefficients, ϵ_0 is the permittivity of free space, S denotes the creation and destruction rates of species. The subscript j indicates the type of species (such as electrons, ions, excited atoms, etc).

In the electron energy equation (4), $n_\varepsilon = n_{\mathrm{e}}\bar{\varepsilon}$ is the electron energy density, $\bar{\varepsilon}=\frac{3}{2}k_{\mathrm{B}}T_{\mathrm{e}}$ is the mean electron energy, and $\boldsymbol{\Gamma}_\varepsilon$ is the electron energy flux density,

$$\boldsymbol{\Gamma}_\varepsilon=-\mu_\varepsilon\mathbf{E}n_\varepsilon-\nabla D_\varepsilon n_\varepsilon. \quad (6)$$

In the source terms of equation (4), the first term describes the Joule heating (or cooling) of electrons in the electric field, the second term, with ν_{ea} denoting the electron-atomic elastic collision frequency, describes the electron energy loss in elastic collisions, and, in the last term, ΔE_k is the energy loss (or gain) due to inelastic collision and R_k is the corresponding reaction rate.

In the energy balance equation (5), c_{p} is the specific heat at constant pressure, ρ is the mass density of the background gas, λ is the thermal conductivity of helium defined as $\lambda = 7.22\times10^{-4}+2.84\times10^{-6}T_{\mathrm{g}}-5.25\times10^{-11}T_{\mathrm{g}}^2$ J cm^{-1} s^{-1} K^{-1} [34].

4.1.2. Transport and reaction rate coefficients. In order to describe the elementary processes in plasma of atmospheric pressure gas discharge in helium we basically followed the approach in [25, 26]. The five effective excited energy levels of the helium atom and two excimer molecular states of helium and two molecular ions are taken into account (table 2). The set of plasma-chemical reactions (table 3) include

- R1: the elastic scattering,
- R2–R6: the direct excitation,
- R7–R17: the stepwise excitation,
- R18: the direct ionization,
- R19–R25: the stepwise ionization,
- R26–R36: the recombination,
- R37–R39: the ion inversion,
- R40: the associative ionization,
- R41: the dissociation,
- R42–R47: the conversion into excimers,
- R48–R50: the de-excitation,
- R51–R78: the Penning ionization,
- R79–R86: the radiation.

Table 2. Species that were considered in the model.

No.	Term	Energy (eV)	Designation
0	He	0	1^1S_0
1	He* (1)	19.82	2^3S_1
2	He* (2)	20.62	2^1S_0
3	He* (3)	20.96	$2^3P_0^0$, $2^3P_1^0$, $2^3P_2^0$
4	He* (4)	21.22	$2^1P_1^0$
5	He* (5)	23.02	3^3S_0, 3^1S_1, $3^3P_2^0$ $3^3P_1^0$, $3^3P_0^0$, 3^3D_3 3^3D_2, 3^3D_1, 3^1D_2
6	He^+	24.59	He^+
7	He_2^*	17.97	He_2 ($^3\Sigma_u^+$)
8	He_2^{**}	18.36	He_2 ($^1\Sigma_g^+$)
9	He_2^+	22.24	He_2^+
10	He_3^+	22.12	He_3^+

The electron mobility, μ_{e}, electron diffusion coefficient, D_{e} and the electron-atomic elastic collision frequency, ν_{ea} are calculated by using the electron energy distribution function obtained from the BOLSIG+ solver and the corresponding collision cross-sections from (see [23])

$$\mu_{\mathrm{e}}=-\frac{\gamma''}{3N}\int_0^\infty\frac{\varepsilon}{\tilde{\sigma}_{\mathrm{m}}}\frac{\partial F_0}{\partial\varepsilon}\,\mathrm{d}\varepsilon \quad (7)$$

and

$$D_{\mathrm{e}}=\frac{\gamma''}{3N}\int_0^\infty\frac{\varepsilon}{\tilde{\sigma}_{\mathrm{m}}}F_0\,\mathrm{d}\varepsilon, \quad (8)$$

and the rate constants from

$$K_{\mathrm{R}}=\gamma''\int_0^\infty\varepsilon\sigma_{\mathrm{R}}F_0\,\mathrm{d}\varepsilon, \quad (9)$$

where R is varying from 1 to 25 in table 3, σ_{R} denotes the corresponding collision cross-section. Data for these collision cross-sections were taken from [35–39]. The rate coefficients for all other reactions (R26–R86 in table 3) were taken from [25, 26]. Here, $\varepsilon = m_{\mathrm{e}}v_{\mathrm{e}}^2/2e$ is the electron kinetic energy, $\tilde{\sigma}_{\mathrm{m}}$ is effective momentum cross-section, N is the background gas density and $\gamma''=\sqrt{2e/m_{\mathrm{e}}}$. F_0 is the electron energy distribution function obtained from the solution of the electron Boltzmann equation. It is normalized as

$$\int_0^\infty F_0(\varepsilon)\sqrt{\varepsilon}\,\mathrm{d}\varepsilon=1. \quad (10)$$

The source terms in the continuity equation (1) are determined by the elementary processes occurring in the plasma, from

$$S_k=\sum_i R_i-\sum_l R_l', \quad (11)$$

where R_i and R_l' are the creation and destruction rates, which are proportional to the constants K_{R} of the corresponding reactions and densities of species involved in these reactions.

Table 3. The set of plasma chemical reactions for helium used in the model. $T_e^{'}$ is the temperature of electrons in eV and T_g is the gas temperatures in K.

Index	Reaction	Rate coefficient	Threshold energy (eV)
R1	$e + He \rightarrow e + He$	Cross section	0
R2	$e + He \leftrightarrow e + He^*$ (1)	Cross section	± 19.82
R3	$e + He \leftrightarrow e + He^*$ (2)	Cross section	± 20.62
R4	$e + He \leftrightarrow e + He^*$ (3)	Cross section	± 20.96
R5	$e + He \leftrightarrow e + He^*$ (4)	Cross section	± 21.22
R6	$e + He \leftrightarrow e + He^*$ (5)	Cross section	± 23.02
R7	$e + He^*$ (1) $\leftrightarrow e + He^*$ (2)	Cross section	± 0.80
R8	$e + He^*$ (1) $\leftrightarrow e + He^*$ (3)	Cross section	± 1.14
R9	$e + He^*$ (1) $\leftrightarrow e + He^*$ (4)	Cross section	± 1.40
R10	$e + He^*$ (1) $\leftrightarrow e + He^*$ (5)	Cross section	± 3.20
R11	$e + He^*$ (2) $\leftrightarrow e + He^*$ (3)	Cross section	± 0.35
R12	$e + He^*$ (2) $\leftrightarrow e + He^*$ (4)	Cross section	± 0.60
R13	$e + He^*$ (2) $\leftrightarrow e + He^*$ (5)	Cross section	± 2.41
R14	$e + He^*$ (3) $\leftrightarrow e + He^*$ (4)	Cross section	± 0.25
R15	$e + He^*$ (3) $\leftrightarrow e + He^*$ (5)	Cross section	± 2.06
R16	$e + He^*$ (4) $\leftrightarrow e + He^*$ (5)	Cross section	± 1.80
R17	$e + He_2^* \leftrightarrow e + He_2^{**}$	Cross section	± 0.39
R18	$e + He \rightarrow 2e + He^+$	Cross section	24.59
R19	$e + He^*$ (1) $\rightarrow 2e + He^+$	Cross section	4.77
R20	$e + He^*$ (2) $\rightarrow 2e + He^+$	Cross section	3.97
R21	$e + He^*$ (3) $\rightarrow 2e + He^+$	Cross section	3.62
R22	$e + He^*$ (4) $\rightarrow 2e + He^+$	Cross section	3.37
R23	$e + He^*$ (5) $\rightarrow 2e + He^+$	Cross section	1.56
R24	$e + He_2^* \rightarrow 2e + He_2^+$	Cross section	4.27
R25	$e + He_2^{**} \rightarrow 2e + He_2^+$	Cross section	3.88
R26	$2e + He^+ \rightarrow He^*$ (1) $+ e$	$4.1 \times 10^{-27} T_e^{'-4.5}$ cm^6 s^{-1}	−4.77
R27	$2e + He^+ \rightarrow He^*$ (2) $+ e$	$1.4 \times 10^{-27} T_e^{'-4.5}$ cm^6 s^{-1}	−3.97
R28	$e + He + He_2^+ \rightarrow He^*$ (1) $+ 2He$	$1 \times 10^{-31} T_e^{'-3.5}$ cm^6 s^{-1}	0
R29	$2e + He_2^+ \rightarrow He_2^* + e$	$5.4 \times 10^{-27} T_e^{'-4.5}$ cm^6 s^{-1}	0
R30	$e + He_2^+ \rightarrow He^*$ (2) $+ He$	$3 \times 10^{-11} T_e^{'-1.5}$ cm^3 s^{-1}	0
R31	$e + He_3^+ \rightarrow He^*$ (2) $+ 2He$	$2.9 \times 10^{-7} T_e^{'-0.5}$ cm^3 s^{-1}	0
R32	$e + He_2^+ \rightarrow He + He^*$ (5)	$5 \times 10^{-10} T_g/(11605 \times T_e^{'})$ cm^3 s^{-1}	0
R33	$2e + He^+ \rightarrow e + He^*$ (5)	$3.59 \times 10^{-27} T_e^{'-4.5}$ cm^6 s^{-1}	−1.56
R34	$e + He + He^+ \rightarrow He + He^*$ (5)	$4.156 \times 10^{-29} T_e^{'-1.5}$ cm^6 s^{-1}	0
R35	$2e + He_2^+ \rightarrow e + He_2^{**}$	$3.59 \times 10^{-27} T_e^{'-4.5}$ cm^6 s^{-1}	0
R36	$e + He + He_2^+ \rightarrow He + He_2^{**}$	$4.156 \times 10^{-29} T_e^{'-1.5}$ cm^6 s^{-1}	0
R37	$He^+ + 2He \rightarrow He_2^+ + He$	$3.017 \times 10^{-29} T_g^{-1}$ cm^6 s^{-1}	0
R38	$He_2^+ + 2He \rightarrow He_3^+ + He$	$3.4 \times 10^{-29} T_g^{-0.75}$ cm^6 s^{-1}	0
R39	$He_3^+ + He \rightarrow He_2^+ + 2He$	$8 \times 10^{-11} T_g^{-1.5} \exp(-1973/T_g)$ cm^3 s^{-1}	0
R40	He^* (5) $+ He \rightarrow e + He + He^+$	1.5×10^{-11} cm^3 s^{-1}	0
R41	$e + He_2^* \rightarrow e + 2He$	3.8×10^{-9} cm^3 s^{-1}	−17.9
R42	He^* (1) $+ 2He \rightarrow He_2^* + He$	$3.23 \times 10^{-33} \exp(-778/T_g)$ cm^6 s^{-1}	0
R43	He^* (2) $+ 2He \rightarrow He_2^{**} + He$	$3.23 \times 10^{-33} \exp(-778/T_g)$ cm^6 s^{-1}	0
R44	He^* (3) $+ 2He \rightarrow He_2^* + He$	$3.23 \times 10^{-33} \exp(-778/T_g)$ cm^6 s^{-1}	0
R45	He^* (4) $+ 2He \rightarrow He_2^{**} + He$	$3.23 \times 10^{-33} \exp(-778/T_g)$ cm^6 s^{-1}	0
R46	He^* (5) $+ 2He \rightarrow He_2^* + He$	$2.42 \times 10^{-33} \exp(-778/T_g)$ cm^6 s^{-1}	0
R47	He^* (5) $+ 2He \rightarrow He_2^{**} + He$	$8 \times 10^{-34} \exp(-778/T_g)$ cm^6 s^{-1}	0
R48	He^* (2) $+ He \rightarrow He^*$ (1) $+ He$	3.6×10^{-15} cm^3 s^{-1}	0
R49	He^* (5) $+ He \rightarrow He^*$ (3) $+ He$	$3.204 \times 10^{-12} T_g^{0.5}$ cm^3 s^{-1}	0
R50	He^* (5) $+ He \rightarrow He^*$ (4) $+ He$	$3.204 \times 10^{-12} T_g^{0.5}$ cm^3 s^{-1}	0
R51	$2He^*$ (1) $\rightarrow e + He + He^+$	2.4×10^{-9} cm^3 s^{-1}	−15.05
R52	He^* (1) $+ He^*$ (2) $\rightarrow e + He + He^+$	2.4×10^{-9} cm^3 s^{-1}	−15.85

(Continued.)

Table 3. (Continued.)

Index	Reaction	Rate coefficient	Threshold energy (eV)
R53	$He^*(1) + He^*(3) \rightarrow e + He + He^+$	2.4×10^{-9} cm^3 s^{-1}	−16.20
R54	$He^*(1) + He^*(4) \rightarrow e + He + He^+$	2.4×10^{-9} cm^3 s^{-1}	−16.45
R55	$He^*(1) + He^*(5) \rightarrow e + He + He^+$	2.4×10^{-9} cm^3 s^{-1}	−18.26
R56	$He^*(1) + He_2^* \rightarrow e + 2He + He^+$	2.5×10^{-9} cm^3 s^{-1}	−13.20
R57	$He^*(1) + He_2^{**} \rightarrow e + 2He + He^+$	2.5×10^{-9} cm^3 s^{-1}	−13.59
R58	$2He^*(2) \rightarrow e + He + He^+$	2.1×10^{-9} cm^3 s^{-1}	−16.64
R59	$He^*(2) + He^*(3) \rightarrow e + He + He^+$	2.1×10^{-9} cm^3 s^{-1}	−16.99
R60	$He^*(2) + He^*(4) \rightarrow e + He + He^+$	2.1×10^{-9} cm^3 s^{-1}	−17.25
R61	$He^*(2) + He^*(5) \rightarrow e + He + He^+$	2.1×10^{-9} cm^3 s^{-1}	−19.05
R62	$He^*(2) + He_2^* \rightarrow e + 2He + He^+$	2.1×10^{-9} cm^3 s^{-1}	−14.00
R63	$He^*(2) + He_2^{**} \rightarrow e + 2He + He^+$	2.1×10^{-9} cm^3 s^{-1}	−14.39
R64	$2He^*(3) \rightarrow e + He + He^+$	2.1×10^{-9} cm^3 s^{-1}	−17.34
R65	$He^*(3) + He^*(4) \rightarrow e + He + He^+$	2.1×10^{-9} cm^3 s^{-1}	−17.59
R66	$He^*(3) + He^*(5) \rightarrow e + He + He^+$	2.1×10^{-9} cm^3 s^{-1}	−19.40
R67	$He^*(3) + He_2^* \rightarrow e + 2He + He^+$	2.1×10^{-9} cm^3 s^{-1}	−14.35
R68	$He^*(3) + He_2^{**} \rightarrow e + 2He + He^+$	2.1×10^{-9} cm^3 s^{-1}	−14.74
R69	$2He^*(4) \rightarrow e + He + He^+$	2.1×10^{-9} cm^3 s^{-1}	−17.85
R70	$He^*(4) + He^*(5) \rightarrow e + He + He^+$	2.1×10^{-9} cm^3 s^{-1}	−19.65
R71	$He^*(4) + He_2^* \rightarrow e + 2He + He^+$	2.1×10^{-9} cm^3 s^{-1}	−14.60
R72	$He^*(4) + He_2^{**} \rightarrow e + 2He + He^+$	2.1×10^{-9} cm^3 s^{-1}	−14.99
R73	$2He^*(5) \rightarrow e + He + He^+$	2.1×10^{-9} cm^3 s^{-1}	−21.46
R74	$He^*(5) + He_2^* \rightarrow e + 2He + He^+$	2.1×10^{-9} cm^3 s^{-1}	−16.41
R75	$He^*(5) + He_2^{**} \rightarrow e + 2He + He^+$	2.1×10^{-9} cm^3 s^{-1}	−16.80
R76	$2He_2^* \rightarrow e + 3He + He^+$	2.1×10^{-9} cm^3 s^{-1}	−11.35
R77	$He_2^* + He_2^{**} \rightarrow e + 3He + He^+$	2.1×10^{-9} cm^3 s^{-1}	−11.74
R78	$2He_2^{**} \rightarrow e + 3He + He^+$	2.1×10^{-9} cm^3 s^{-1}	−12.13
R79	$He^*(3) \rightarrow He$	1×10^7 s^{-1}	0
R80	$He^*(4) \rightarrow He$	1.8×10^9 s^{-1}	0
R81	$He^*(5) \rightarrow He$	9.1×10^7 s^{-1}	0
R82	$He^*(3) \rightarrow He^*(1)$	1.022×10^7 s^{-1}	0
R83	$He^*(4) \rightarrow He^*(2)$	1.97×10^6 s^{-1}	0
R84	$He^*(5) \rightarrow He^*(3)$	2.94×10^7 s^{-1}	0
R85	$He^*(5) \rightarrow He^*(4)$	9.79×10^6 s^{-1}	0
R86	$He_2^{**} \rightarrow 2He$	6×10^8 s^{-1}	0

4.1.3. Boundary Conditions. The schematic of the computational domain, which is rectangular in shape, is shown in figure 6. The boundary conditions applied on the cathode ($z = 0$) and anode ($z = d$) are listed in table 4. In the boundary conditions, $\upsilon_j = \sqrt{8k_B T_j/\pi m_j}$ denotes the thermal velocity of species of type j, γ is the secondary electron emission (SEE) coefficient, $T_0 = 300$ K is the background (room) temperature, and $\hat{\mathbf{n}}$ is the outward normal unit vector.

We set the value of the secondary emission coefficient equal to $\gamma = 0.1$ for all ionic species. The switching function a is set equal to one if the electric field is directed towards the boundary, otherwise, it is equal to zero.

We specified the gas temperature $T_g = T_c$ on the cathode and imposed the boundary conditions in the form of convective cooling (see table 4) on the anode and dielectric wall ($r = l$).

The surface charge density σ is calculated from

$$\frac{\partial \sigma}{\partial t} = \hat{\mathbf{n}} \cdot \mathbf{J}, \tag{12}$$

where $\mathbf{J}$ is the current density.

The symmetry condition ('normal flow is set to zero') is applied to all dependent variables on the symmetry axis.

Finally, the DC voltage U_d is obtained from the external circuit equation

$$\frac{dU_d}{dt} + \frac{1}{C}\left(I_d - \frac{U_{src} - U_d}{R}\right) = 0, \tag{13}$$

where I_d is the discharge current, C is the capacitance, R is the resistance and U_{src} is the source voltage. We set $U_{src} = 500$ V and $C = 1$ pF in the calculations.

4.2. Numerical results

4.2.1. 1D approach. Calculations are carried out for helium APGD with parameters in accordance with the experimental data in table 1. The pressure is defined as atmospheric, $p = 760$ Torr, and the discharge gap is $d = 10$ mm. More specifically, table 1 includes two parameter sets, corresponding to regimes

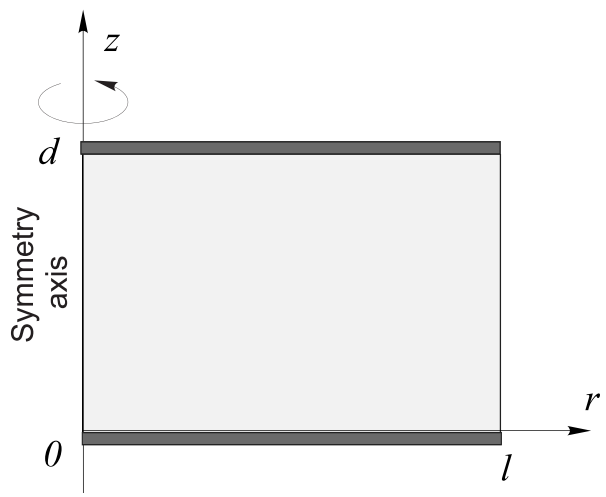

Figure 6. Schematic representation of the planar gas discharge cell.

with cooled and uncooled cathode, where the cathode temperature and the discharge current density on the cathode are as follows:

- $T_c = 400$ K, $J_c = 2.3$ A cm^{-2},
- $T_c = 800$ K, $J_c = 0.4$ A cm^{-2}.

The spatial profiles of the electron density n_e and the sum of ionic species density n_i (a), the electric field E (b), and the electric potential ϕ (c) in the cathode sheath region of helium APGD are depicted in figure 7. Two different regimes with cathode temperatures $T_c = 400$ K and 800 K are shown. The dotted vertical lines in this figure indicate the sheath layer boundaries, identified as points at which the electron density is equal to half of the total ion density, $n_e = 0.5\,n_i$. According to the calculations, the cathode sheath thickness increases from 62 μm to 111 μm with the increase in the cathode temperature from $T_c = 400$ K to 800 K. This trend as well as the values of the cathode layer thickness are in good agreement with the experimental observations for helium APGD (see figure 7). However, as it can be seen from figure 7(b), the values of electric field on the cathode surface decrease from $E_c = 79$ to 38 kV cm^{-1} as the temperature of the cathode increases, while the experimental value of $E_c \approx 60$ kV cm^{-1} in figure 7 stays unchanged. Nevertheless, the experimental and calculated values of E_c are close to each other, and the discrepancy is an inevitable consequence of the insufficiency of 1D model for describing essentially two-dimensional effects.

4.2.2. 2D approach: I. In this section, calculations are carried out again for the two parameter sets, corresponding to helium APGD regimes with cooled and uncooled cathode from table 1, however, this time on the basis of the 2D model. More specifically, the helium pressure is defined as atmospheric, $p = 760$ Torr, the discharge gap is $d = 10$ mm, the radius of the discharge tube is $l = 8$ mm, the cathode temperature and discharge current are specified according to the experimental values $T_c = 400$ K for cooled and 800 K and for uncooled cathode. The discharge current in both cases is $I_d = 1$ A.

Note that figure 7 also includes axial profiles of the electric field magnitude $|\mathbf{E}|$ (a), particle (ion and electron) densities (b), and electric potential ϕ (c), obtained for cathode temperatures of $T_c = 400$ K and 800 K, from the 2D model. In agreement with the experimental observations (see figure 7(b)) (and also in agreement with the 1D calculations), the cathode sheath thickness increases with the increase in the cathode temperature from $T_c = 400$ K to 800 K. Corresponding values of the electric field and thicknesses of the cathode sheath are sufficiently close to those observed for helium APGD in the experiment (see figure 7(c)). It should also be noted from figure 7(c) that the cathode fall voltage, in accordance with the experiment, and in contrast to 1D model, the reliability of which is obviously limited compared to a more adequate 2D model, demonstrates an increase with increasing the cathode temperature.

In fact, 2D model demonstrates the formation of a discharge with a typical non-uniform positive column, which is the result of intensive heating of the gas in the bulk of the discharge. The right-hand side of the heat equation (5) includes two terms, which are responsible for the Joule heating of a neutral gas and heating due to elastic electron-atom collisions. The first term predominates in the (cathode) space charge sheath, while the collisional heating predominates in a quasi-neutral plasma. In the case of a sufficiently long glow discharge (which is our case, because the thickness of the cathode sheath is of the order of fractions of a mm and the gas gap is 10 mm), the total heating of the gas is determined by its heating by the quasi-neutral plasma, that is, by the second term. The resulting axial profile of the electron density n_e, as well as the total ion density n_i (plasma is quasi-neutral in the relevant region, $n_e \approx n_i$) reveals two local maxima in the negative glow and the anode glow, between which n_e gradually increases by several times.

4.2.3. 2D approach: II. In this section, we focus on the discharge conditions in section 3, where APGDs were analyzed in the constricted mode with cooled and uncooled cathodes as well as in the diffuse mode. Correspondingly, we defined the discharge gap $d = 5$ mm, the radius of the discharge tube $l = 18$ mm, the cathode temperature was specified according to the experimental values: $T_c = 400$ K for cooled and 800 K for uncooled cathode and $T_c = 700$ K in the case of the diffuse discharge (see figure 4). The discharge current is $I_d = 1$ A in all cases.

Computed two-dimensional profiles of the electron density n_e (first row), the total ion density n_i (second row), and the magnitude of the current density $|\mathbf{J}|$ (third row) for these discharge regimes are shown in figure 8. In this figure, the first and second columns correspond to the constricted discharges with cooled and uncooled cathodes, respectively, and the third column corresponds to the diffuse discharge. Notice that the logarithmic scale was applied along the (vertical)

Table 4. Boundary conditions on the cathode and anode used in the model.

Species type	Cathode ($z=0$)	Anode ($z=d$) and dielectric wall ($r=l$)
Electrons, n_e	$\hat{\mathbf{n}}\cdot\mathbf{\Gamma}_e=\frac{1}{4}\upsilon_e n_e-\gamma\sum_j\hat{\mathbf{n}}\cdot\mathbf{\Gamma}_j$	$\hat{\mathbf{n}}\cdot\mathbf{\Gamma}_e=\frac{1}{4}\upsilon_e n_e$
He ions, n_i	$\hat{\mathbf{n}}\cdot\mathbf{\Gamma}_i=\frac{1}{4}\upsilon_i n_i+a n_i\mu_i(\hat{\mathbf{n}}\cdot\mathbf{E})$	$\hat{\mathbf{n}}\cdot\mathbf{\Gamma}_i=\frac{1}{4}\upsilon_i n_i+a n_i\mu_i(\hat{\mathbf{n}}\cdot\mathbf{E})$
He excited states, n_m	$\hat{\mathbf{n}}\cdot\mathbf{\Gamma}_m=\frac{1}{4}\upsilon_m n_m$	$\hat{\mathbf{n}}\cdot\mathbf{\Gamma}_m=\frac{1}{4}\upsilon_m n_m$
Electron energy density, n_ε	$\hat{\mathbf{n}}\cdot\mathbf{\Gamma}_\varepsilon=\frac{1}{3}\upsilon_e n_\varepsilon-2k_B T_e\gamma\sum_j\hat{\mathbf{n}}\cdot\mathbf{\Gamma}_j$	$\hat{\mathbf{n}}\cdot\mathbf{\Gamma}_\varepsilon=\frac{1}{3}\upsilon_e n_\varepsilon$
Electric potential, ϕ	$\phi=0$	$\phi=U_d$ ($z=d$) and $\hat{\mathbf{n}}\cdot\nabla\phi=\frac{1}{\varepsilon_0}\sigma$ ($r=l$)
Gas temperature, T_g	$T_g=T_c$	$\hat{\mathbf{n}}\cdot\lambda\nabla T_g=h(T_0-T_g)$

axial direction to display the near-cathode region. In fact, the cathode sheath in the constricted mode is very narrow and has a thickness of about 0.1 mm. The characteristic regions of the glow discharge can be clearly identified. These are the cathode dark space, the negative glow, the Faraday dark space, and the non-uniform positive column (cf figure 1). Note that the discharge with the uncooled cathode (second column in figure 8) covers a greater cathode surface area, compared to the discharge with the cooled cathode (first column in figure 8), in consistency with the experimental observations depicted in figure 1. In the diffuse mode, the discharge occupies most of the interelectrode region (third column in figure 8).

4.2.4. Agreement between the modelling and experiment. In general, the numerical model adequately (both qualitatively and to some extent quantitatively) describes the discharge parameters, specifically, in the cathode sheath. First of all, as we noted above, these are the magnitude and the profile of the electric field in the cathode sheath (see figure 7(b)). Correspondingly, the experimental value of the cathode layer thickness is well reproduced by the model (see figure 7(b)) and it is in agreement with the literature (see, e.g. [40], page 182). A (qualitative) agreement between the experimental and computed (for the discharge with gas gap $d=5$ mm) radial profiles of the electric field along the cathode surface can be seen seen in figure 9(a). Note from this figure that the computed electric field at $r=0$ (on the axis) for both cases with cooled and uncooled cathode practically coincide at $z=0$ (on the cathode surface) with corresponding values computed for the discharge with a gas gap $d=10$ mm (see figure 7(b)), which is to be expected.

Furthermore, the value of the normal current density (see figure 9(b)) is in good agreement with experimental data (table 1) and that reported in the literature (e.g. [40], page 183). In the case of the cathode temperature $T_c=400$ K, the axial value of the current density on the cathode surface, computed from the 2D model $J_c=2.23$ and 2.51 A cm^{-2} for APGDs with gas gaps of $d=10$ and 5 mm, respectively) practically coincides with that observed in the experiment (see table 1). Consequently, since J_c computed from the 1D model is equal to the corresponding experimental value (the discharge regime in 1D model was selected to produce the experimental current density), one can observe an almost exact coincidence of the (axial) discharge characteristics obtained from the 1D and 2D models for the case of a cooled cathode (see figures 7(a) and (b)).

Further, the value of the current density in the positive column of the constricted APGD is close to that of 20 A cm^{-2} observed in the experiment (see table 1 and first two panels in the third row in figure 8).

However, the model, in comparison with the experiment, reproduces a somewhat larger value of the voltage drop in the cathode layer (cf table 1 and figure 7(c)). An exact match of the voltage drop can be achieved by choosing a suitable value of the SEE γ. However, the fitting of the experimental parameters was not the purpose of this study: $\gamma=0.1$ was used for all calculations. In fact, the effective value of the SEE from the cathode is one of the main sources of uncertainty in fluid models of glow discharges. It depends nonlinearly on the reduced electric field, E/N, and also on the material of the cathode, and even on the state of the cathode surface (see, e.g. [41]). In fact, the SEE coefficient is often used as a fitting parameter in numerical models to fit computed data to measured data.

Furthemore, the model implemented in this work predicts gas temperatures to be higher than those measured in the relevant experiments for the helium APGD (see figure 10). In these experiments, the gas flow rate was quite small (not greater than 1 l/min), and therefore its contribution is considered negligible in the numerical model. It is very possible that taking into account the gas flow, although it would greatly complicate an already complicated model, will lead to more accurate gas temperature values.

In addition, it should be mentioned that, under certain parameter regimes, the simulations exhibit the emergence and multiplication of current structures (cathode spots). These structures are visibly similar to those observed in the experiment [12].

It is also worth mentioning an interesting observation associated with the existence of multiple solutions to this sort of problems. Namely, by implementing an existing solution of the diffuse regime (see the third column in figure 8), which is dynamically unstable, as the initial condition, and carrying out calculations, the solution is usually drawn away from this initial state and converges to the constricted regime (the first two columns in figure 8). The reason for that could be a modification in the numerical grid or numerical solution method, which plays the role of perturbation, that leads to a destabilization of this state.

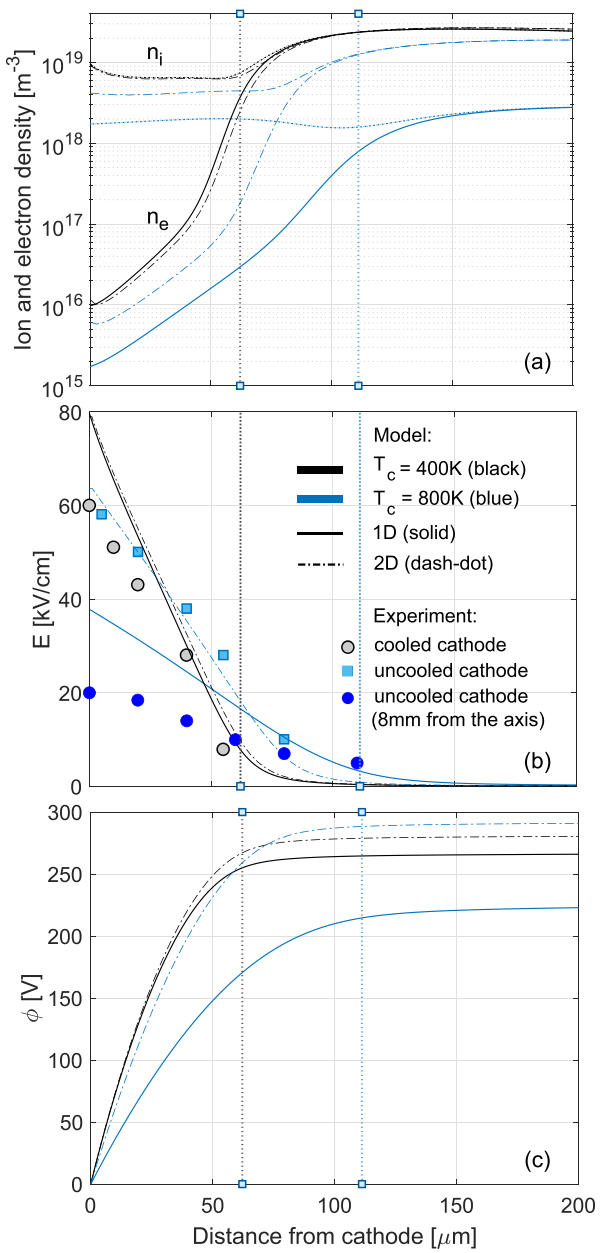

Figure 7. Computed from 1D and 2D models axial profiles of the electron and the sum of ionic species densities n_e and n_i (a), electric field $|\mathbf{E}|$ (b), and potential ϕ (c) in helium APGD, obtained for cathode temperatures $T_c = 400$ and 800 K. The pressure is $p = 760$ Torr, the gas gap is $d = 10$ mm, the radius of the discharge tube is $l = 8$ mm, the discharge current is $I_d = 1$ A. In the case of 1D, the regimes with current densities $J = 2.3$ A cm^{-2} (for $T_c = 400$ K) and 0.4 A cm^{-2} (for $T_c = 800$ K) were selected, according to the experimental values in table 1. Vertical lines indicate the cathode layer thicknesses (obtained from 1D).

5. Discussions

Summarizing the experimental and simulation observations, the following statements can be established:

(a) In a normal DC APGD with a constricted positive column (i.e. the width of the positive column is less than the width of the negative glow) heating the cathode due to a current flow leads to an increase in the interelectrode voltage compared to that of the discharge with a cooled cathode. This increase occurs due to a change in the cathode fall voltage. In the case of the external heating of the cathode, the interelectrode voltage decreases. For example, in helium APGD with an uncooled cathode at a current of 1 A and a gap of 10 mm the interelectrode voltage is about 80 V greater than in a discharge with a cooled cathode. At the same time, heating the cathode with an external heat source leads to a decrease in voltage by 20–30 V at a current of 50 mA.

(b) The magnitude of the reduced electric field can be estimated using the values of the gas temperature from table 1 and the values of the electric field strength close to the cathode surface (see figure 7(c)). Near the surface of the cooled cathode, it is equal to 320 Td. For an uncooled cathode it is about 640 Td on the axis and 215 Td at the periphery (at a distance of 8 mm from the axis).

(c) The effect of SEE from the cathode seems to be directly related to the analysis carried out here. Indeed, the cathode fall voltage is apparently affected by the SEE coefficient. It should be noted that a decrease in this coefficient leads to an increase in the cathode fall voltage. The SEE coefficient used in glow discharge models is an effective parameter that takes into account various possible secondary emission processes including ion impact, metastable impact and photoemission [41–43]. From an analysis of experimental data, Phelps and Petrovic [41] have deduced the effective γ as a function of the reduced field strength at the cathode, E/N. This parametrization reflects the relative importance of different electron emission processes under different discharge conditions and also incorporates possible effects due to ionization near the cathode caused by heavy particles (ions or neutrals). In addition, it should be mentioned that the calculations [14, 16] as well as the numerical results obtained from more detailed model and presented in this work, which employed a constant γ, also predict an increase in the operating voltage for a given current with increasing temperature.

(d) The heating of the cathode is usually accompanied by the formation of oxide films on its surface. As it is known from the literature, oxide films can cause an increase or decrease in the SEE coefficient and, as a consequence, a change in the cathode fall voltage. However, even in the case when oxide films are not formed, the same effect of cathode heating to the electrode voltage is still observed. Specifically, the cathode fall voltage increases when the cathode is heated by the discharge current and decreases when it is heated by an external heat source. A mention should be made of [44], which describes an experiment with rapid (less than 1 s) heating of a tungsten wire cathode, in which the development of oxide films is unlikely. Generally, in experiments, the cathode is cleaned as a result of its sputtering when the discharge transits to the arc mode with a thermionic cathode. When the tungsten cathode was heated to white hot for less than 1 s, an increase in the interelectrode voltage by 60–70 V was observed [44].

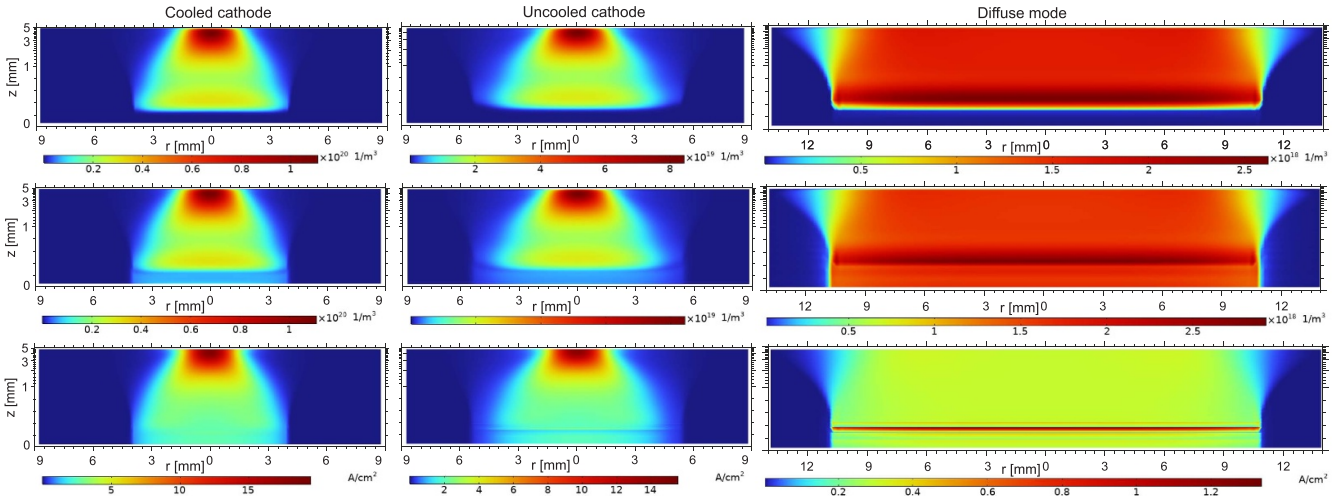

Figure 8. Computed electron density n_e (1st row), total ion density n_i (2nd row) and electric current density $|\mathbf{J}|$ (3rd row) for APGDs with cooled (1st column) and uncooled (2nd column) cathodes and APGD in the diffuse mode (3rd column). The pressure is $p = 760$ Torr, the gas gap is $d = 5$ mm, the radii of the electrodes are $l = 18$ mm, and the discharge current is $I_d = 1$ A.

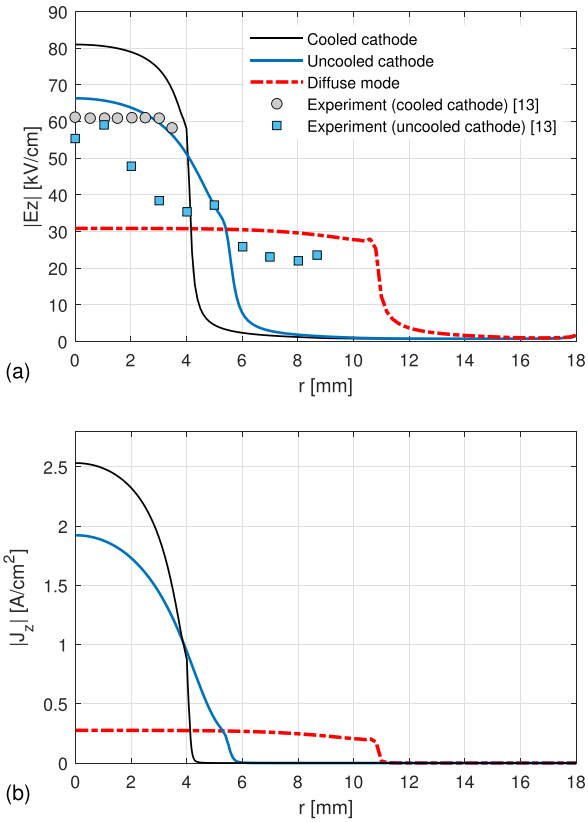

Figure 9. Radial profiles of the computed and experimental electric field (a) and computed current density (b) along the cathode surface, for APGDs with cooled and uncooled cathodes and APGD in the diffuse mode. The conditions are identical to those in figure 8.

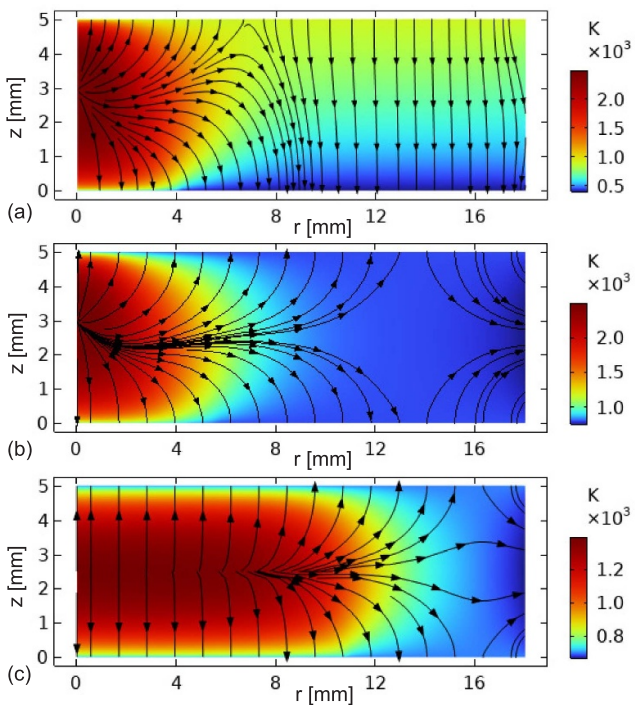

Figure 10. Computed gas temperature profiles and heat flow lines for APGDs with (a) cooled and (b) uncooled cathodes and APGD in the diffuse mode (c). Maximum values of magnitudes of the heat flows in panels (a), (b), and (c) are 640, 510, and 52 W cm^{-2}, respectively. The conditions are identical to those in figure 8.

(e) It should be pointed out that fitting the discharge parameters obtained from the experiment by a numerical model is not aimed in this work. In fact, correlation between the computed and experimental results can be improved by choosing an appropriate SEE coefficient γ. Nevertheless, the numerical models used in this study exhibit good qualitative and, to some extent, quantitative agreement with experimental observations, for discharge regimes with cooled and uncooled cathodes.

6. Conclusions

On the basis of experimental and numerical studies, it was established that the heating of the uncooled cathode, which occurs only as a result of the discharge current flow in a normal DC APGD with a constricted positive column, is accompanied by an increase in the interelectrode voltage and a slight decrease in the electric field in close proximity to cathode surface. On the contrary, additional heating of the cathode by an external heat source leads to a decrease in the interelectrode voltage. The heat flow from the constricted positive column towards the cathode leads to a non-uniform distribution of the electric field on the cathode surface, specifically, an electric field strength is larger at the center and smaller by a factor of 3 at the periphery of the cathode fall layer. It is different from the case with a cooled cathode, where an electric field strength is constant along the cathode surface.

The parameters in the whole cathode region in a diffuse APGD and at the cathode fall periphery of discharge with a constricted positive column more or less obey the scaling laws. However, these parameters deviate from the scaling laws at the center of the cathode region of discharge with the constricted positive column due to an increase in the cathode fall voltage. This increase in the cathode fall voltage (and interelectrode voltage) occurs due to an increase in the thickness of cathode fall layer, which is due to the increase in gas temperature at the cathode fall layer, which is caused by a heat flux from the constricted positive column.

Numerical models are spatially one- and two-dimensional and based on the drift-diffusion theory of gas discharges. Simulations demonstrated good qualitative and, to some degree, quantitative agreement with experimental observations for the discharge regimes with cooled and uncooled cathodes.

Summing up, it should be noted that a deeper insight into the effect of SEE from the cathode in the present context calls for further investigations. Indeed, it seems appropriate to carry out numerical experiments using a more adequate emission coefficient γ, defined as a function of the reduced electric field (the electric field value divided by the background gas density, E/N). However, such an approach is currently limited by the lack of relevant experimental data for helium.

Data availability statement

All data that support the findings of this study are included within the article (and any supplementary files).

Acknowledgment

This work was supported by the Grant F22TUB-003 from the Belarusian Republican Foundation for Fundamental Research and by the Grant 221N363 from the Scientific and Technological Research Council of Türkiye (TUBITAK).

ORCID iDs

Leanid Simonchik https://orcid.org/0000-0002-4854-9225
Ismail Rafatov https://orcid.org/0000-0002-8303-9204

References

[1] Massines F, Rabehi A, Decomps P, Gadri R B, Ségur P and Mayoux C 1998 *J. Appl. Phys.* **83** 2950–7
[2] Kunhardt E E 2000 *IEEE Trans. Plasma Sci.* **28** 189–200
[3] Napartovich A 2001 *Plasmas Polym.* **6** 1–14
[4] Bogaerts A, Neyts E, Gijbels R and Van der Mullen J 2002 *Spectrochim. Acta* B **57** 609–58
[5] Gadri R B *et al* 2000 *Surf. Coat. Technol.* **131** 528–41
[6] Becker K, Schoenbach K and Eden J 2006 *J. Phys. D: Appl. Phys.* **39** R55
[7] Andrade F J, Wetzel W C, Chan G C Y, Webb M R, Gamez G, Ray S J and Hieftje G M 2006 *J. Anal. At. Spectrom.* **21** 1175–84
[8] Mezei P, Cserfalvi T and Janossy M 2001 *J. Phys. D: Appl. Phys.* **34** 1914
[9] Staack D, Farouk B, Gutsol A and Fridman A 2008 *Plasma Sources Sci. Technol.* **17** 025013
[10] Arkhipenko V, Kirillov A, Safronau Y A, Simonchik L and Zgirouski S 2009 *Plasma Sources Sci. Technol.* **18** 045013
[11] Arkhipenko V, Kirillov A, Safronau Y A and Simonchik L 2010 *Eur. Phys. J.* D **60** 455–63
[12] Arkhipenko V, Zgirovskii S, Kirillov A and Simonchik L 2002 *Plasma Phys. Rep.* **28** 858–65
[13] Arkhipenko V, Kirillov A, Safronau Y A, Simonchik L and Zgirouski S 2008 *Plasma Sources Sci. Technol.* **17** 045017
[14] Bogaerts A, Gijbels R and Serikov V V 2000 *J. Appl. Phys.* **87** 8334–44
[15] Arkhipenko V and Simonchik L 2015 *Proc. 32th ICPIG (Iasy, Romania, July 2015) (Iasy, Romania)*
[16] Revel I, Pitchford L and Boeuf J 2000 *J. Appl. Phys.* **88** 2234–9
[17] Kasik M, Michellon C and Pitchford L 2002 *J. Anal. At. Spectrom.* **17** 1398–9
[18] Cvetanović N, Obradović B and Kuraica M 2006 *Czech. J. Phys.* **56** B678–83
[19] Cech J, Brablec A, Stahel P and Cermak M 2007 *Proc. 28th ICPIG (Prague, Czech Republic, July 2007) (Prague, Czech Republic)*
[20] Bondarenko G, Kristya V and Supelnyak M 2012 *Vacuum* **86** 854–6
[21] Phelps A 2001 *Plasma Sources Sci. Technol.* **10** 329
[22] Boeuf J P and Pitchford L C 1995 *Phys. Rev.* E **51** 1376–90
[23] Hagelaar G J M and Pitchford L C 2005 *Plasma Sources Sci. Technol.* **14** 722–33
[24] Rafatov I, Bogdanov E and Kudryavtsev A 2012 *Phys. Plasmas* **19** 033502
[25] Bogdanov E, Kapustin K, Kudryavtsev A and Chirtsov A 2010 *Tech. Phys.* **55** 1430–42
[26] Rafatov I, Islamov G, Eylenceoglu E, Yesil C and Bogdanov E 2023 *Phys. Plasmas* **30** 093504
[27] Foster S J 1927 *Proc. R. Soc.* A **117** 137–63
[28] Kuraica M and Konjević N 1997 *Appl. Phys. Lett.* **70** 1521–3
[29] Arkhipenko V, Zgirovskii S, Konjevic N, Kuraica M and Simonchik L 2000 *J. Appl. Spectrosc.* **67** 910–8
[30] Arkhipenko V, Zgirovskii S, Kirillov A and Simonchik L 2007 *Spectroscopy of Plasma and Natural Objects* (Belaruskaja Navuka) pp 10–66

[31] Baranov G and Smirnov S 1999 *Tech. Phys.* **44** 1305–11
[32] COMSOL Multiphysics v. 6.1 2022 COMSOL AB (available at: www.comsol.com)
[33] Grubert G, Becker M and Loffhagen D 2009 *Phys. Rev.* E **80** 036405
[34] Wang Q, Economou D J and Donnelly V M 2006 *J. Appl. Phys.* **100** 023301
[35] Phelps database (available at: www.lxcat.net/Phelps) (Accessed 1 July 2022)
[36] Pérès I, Alves L and Margot J 1999 *Plasma Chem. Plasma Process* **19** 467
[37] Kato T, Itikawa Y, Ichikawa Y and Sakimoto K 1992 *Research Report NIFS-Series*
[38] Eckstrom D, Nakano H, Lorents D, Rothem T, Betts J, Lainhart M, Dakin D and Maenchen J 1988 *J. Appl. Phys.* **64** 1679–90
[39] Vriens L, Keijser R and Ligthart F 1978 *J. Appl. Phys.* **49** 3807–13
[40] Raizer Y 2011 *Gas Discharge Physics* (Springer)
[41] Phelps A and Petrovic Z L 1999 *Plasma Sources Sci. Technol.* **8** R21
[42] Auday G, Guillot P, Galy J and Brunet H 1998 *J. Appl. Phys.* **83** 5917–21
[43] Eylenceoğlu E, Rafatov I and Kudryavtsev A 2015 *Phys. Plasmas* **22** 013509
[44] Arkhipenko V, Zgirovskii S, Simonchik L and Stel'Makh G 2004 *J. Appl. Spectrosc.* **71** 107–14